Magnetic properties of $S = \frac{1}{2}$ distorted $J_1 - J_2$ honeycomb lattice compound $NaCuIn(PO_4)_2$

V. K. Singh,[1] J. Link,[2] K. Kargeti,[3] M. Barik,[4] B. Lenz,[5] N. Saraswat,[3] U. Jena,[4] I. Heinmaa,[2] P. Khuntia,[4,6] K. Boya,[1] S. K. Panda,[3] R. Stern,[2] Y. Bitla,[7] T. Chakrabarty,[8,*] and B. Koteswararao[1,†]

[1]*Department of Physics, Indian Institute of Technology Tirupati, Tirupati 517506, India*
[2]*National Institute of Chemical Physics and Biophysics, 12618 Tallinn, Estonia*
[3]*Department of Physics, Bennett University, Greater Noida, Uttar Pradesh 201310, India*
[4]*Department of Physics, Indian Institute of Technology Madras, Chennai 600036, India*
[5]*IMPMC, Sorbonne Université, CNRS, MNHN, 4 place Jussieu, 75005 Paris, France*
[6]*Quantum Centre of Excellence for Diamond and Emergent Materials, Indian Institute of Technology Madras, Chennai 600036, India*
[7]*Department of Physics, Central University of Rajasthan, Ajmer, Rajasthan 305817, India*
[8]*Division of Sciences, Krea University, Sri City, Andhra Pradesh 517646, India*

(Received 16 January 2023; revised 13 April 2023; accepted 7 June 2023; published 21 June 2023)

The subtle interplay between low-dimensionality and spin correlations can lead to exotic ground states with unconventional excitations in two-dimensional honeycomb-lattice-based quantum magnets. Herein, we present the structural, magnetic, and heat capacity measurements; density functional theory + Hubbard U (DFT + U) based electronic structure calculations; and quantum Monte Carlo simulations for $NaCuIn(PO_4)_2$. The structure of $NaCuIn(PO_4)_2$ consists of a well-separated, $S = \frac{1}{2}$ distorted J_1-J_2 honeycomb layer which is a combination of the magnetic couplings J_1 (forming spin dimers) and J_2 (constituting spin chains). At high temperatures, the magnetic susceptibility $\chi(T)$ follows paramagnetic behavior with a Curie-Weiss temperature $\theta_{CW} \approx -16$ K, implying the presence of antiferromagnetic interactions. A broad maximum is observed at about 13 K in $\chi(T)$, indicating the presence of short-range spin correlations. The quantum Monte Carlo simulations using the $S = \frac{1}{2}$ J_1-J_2 Heisenberg model on a distorted honeycomb lattice are in good agreement with the measured magnetic susceptibility data. The obtained ratio of the exchange couplings ($\frac{J_2}{J_1}$) is 2.63, which is consistent with the value obtained from our DFT + U calculations. The title material undergoes a magnetic long-range order at 0.4 K in the heat capacity, which is suppressed with an applied magnetic field of 10 kOe. The magnetic heat capacity data follow a linear temperature-dependent behavior well above the transition temperature, suggesting the presence of gapless excitations. The observed behavior can be attributed to the presence of low connectivity and weak magnetic frustration in this two-dimensional distorted honeycomb lattice.

DOI: 10.1103/PhysRevB.107.214430

I. INTRODUCTION

The interplay between low-dimensionality and spin correlations can stabilize exotic states in quantum magnets. The discovery of high-temperature superconductivity in layered two-dimensional (2D) cuprates has been a breakthrough in the field of condensed matter physics [1]. The investigation of 2D quantum magnetism in $S = \frac{1}{2}$ Heisenberg antiferromagnetic (HAFM) spin systems has gained significant attention due to the presence of inherent quantum fluctuations. Understanding the nature of the ground state and associated excitations in low-dimensional quantum magnets continues to be a topic of much recent interest [2,3]. The $S = \frac{1}{2}$ HAFM square lattice is one of the most studied models both theoretically and experimentally, and it exhibits a long-range order (LRO) in the ground state at $T = 0$ K [4–6]. The scenario becomes further interesting in the case of the $S = \frac{1}{2}$ HAFM honeycomb lattice. Although the ground state stabilizes Néel order, the quantum fluctuations are more robust in the $S = \frac{1}{2}$ 2D HAFM honeycomb lattice due to the low coordination number ($z = 3$) associated with the 2D honeycomb lattice compared to the 2D square lattice ($z = 4$) [7]. These enhanced quantum fluctuations suppress the magnetic moment per site in the honeycomb lattice. As a result, the ordered state can be destabilized, and an exotic disordered phase can be induced by minor lattice distortions and anisotropies [8–12]. Interestingly, the 2D honeycomb geometry, in which various perturbations such as bond-dependent Kitaev-type interactions, spin-orbit coupling, the involvement of second-nearest-neighbor interactions, and the randomness of the magnetic exchange couplings play a role, can host quantum spin liquids with exotic excitations [13–18]. However, only a handful of prototype compounds are available in the $S = \frac{1}{2}$ HAFM honeycomb lattice category. Several materials with the distorted $S = \frac{1}{2}$ HAFM honeycomb lattice exhibiting nontrivial ground states were reported recently. A few such candidates are $Yb_2Si_2O_7$ [19,20], $CuAl(AsO_4)O$ [21], $Zn(hfac)_2A_xB_{1-x}$ (the hfac represents 1,1,1,5,5,5-hexafuoroacetylacetonate) [22], and $Cu_2(pymca)_3(ClO_4)$ (the pymca represents pyrimidine-2-carboxylate) [23–25]. It is fascinating to see that the ground state for most of these distorted honeycomb lattice materials shows gapped and gapless states. The rare-earth material $Yb_2Si_2O_7$ is an example of a spin-gapped system, having a

*tanmoy.chakrabarty@krea.edu.in
†koteswararao@iittp.ac.in

spatially distorted honeycomb lattice with the magnetic couplings J_1 and J_2. Here, the ratio of the exchange couplings in the distorted honeycomb layer ($\frac{J_2}{J_1}$) is about 0.4, which locates the system in the quantum spin-gapped ground state [19]. In addition, the magnetic field-induced successive Bose-Einstein condensation phase transitions are also observed in this $4f$ ion-based honeycomb material. The compound $CuAl(AsO_4)O$ appears to be in the valence-bond solid ground state with a large spin gap of 350 K, where the quantum state may be elucidated as a collection of dimer units with a very small inter- to the intradimer ratio of 0.01 on a distorted honeycomb lattice background [21]. On the other hand, there is a gapless liquidlike behavior reported in the organic compound $Zn(hfac)_2A_xB_{1-x}$ [22], which hosts complex and distorted couplings on a 2D honeycomb lattice. The compound $Cu_2(pymca)_3(ClO_4)$ has been reported to be another type of distorted honeycomb lattice copper compound that shows no long-range magnetic order down to 2 K and shows the spin-gapped ground state in the spin excitation spectrum. The presence of magnetic plateaus has also been observed in external applied magnetic fields up to 70 T [24,25].

In this context, exploring novel low-dimensional quantum magnetism in distorted honeycomb lattice structures seems an appealing setting. Herein, we report a detailed investigation of the $S = \frac{1}{2}$ magnetic system $NaCuIn(PO_4)_2$, where the spins Cu^{2+} are arranged on a distorted 2D honeycomb lattice. The nearest-neighbor (NN) coupling J_1 forms spin dimers, and the second-NN coupling J_2 constitutes spin chains. The magnetic data analysis based on quantum Monte Carlo (QMC) simulations on a distorted J_1-J_2 honeycomb lattice followed by density functional theory (DFT) electronic structure calculations confirms the presence of both couplings. The estimated ratio of magnetic couplings between Cu^{2+} ions has been found to be $\frac{J_2}{J_1} \approx 2.63$. The weak interlayer couplings imply that $NaCuIn(PO_4)_2$ has well-separated $S = \frac{1}{2}$ distorted J_1-J_2 honeycomb layers. The interaction between Cu^{2+} ($S = \frac{1}{2}$) ions is predominantly antiferromagnetic (AFM) in nature, as evidenced by the Curie-Weiss temperature $\theta_{CW} \approx -16$ K. The heat capacity $C_p(T)$ shows an anomaly at 0.4 K, which indicates the presence of an AFM phase transition in $NaCuIn(PO_4)_2$. Interestingly, linear behavior in the temperature-dependent magnetic heat capacity $C_m(T)$ above the AFM phase transition implies the presence of gapless excitations in $NaCuIn(PO_4)_2$. The magnetic coupling ratio ($\frac{J_2}{J_1} \approx 2.63$) places the compound $NaCuIn(PO_4)_2$ on the Néel side of the quantum phase diagram (QPD), a bit far away from the quantum critical point (QCP) [10,26].

II. METHODS

A polycrystalline sample of $NaCuIn(PO_4)_2$ was synthesized using the conventional solid-state synthesis technique. High-purity CuO (Aldrich, 99.99%), Na_2CO_3 (Aldrich, 99.99%), $(NH_4)_2H(PO_4)$ (Aldrich, 99.5%), and In_2O_3 (Aldrich, 99.9%) were mixed in a stoichiometric proportion and ground thoroughly using an agate mortar and pestle. The mixture was then pelletized and heated at 300 °C, 400°C, 500 °C, respectively, firing at each step for 6 h. The final firing was done at 870 °C for 48 h with two intermediate grindings. To get the single phase, 5% more Na_2CO_3 is added to compensate for the evaporation of Na from the composition. The phase purity of the sample was confirmed by powder x-ray diffraction (XRD) measurements performed at room temperature. For the powder XRD experiment, a PANalytical powder diffractometer with Cu $K\alpha$ radiation ($\lambda_{avg} \approx 1.54$ Å) was used. Rietveld refinement analysis was done using the FULLPROF SUITE software package [27]. The temperature (2–300 K) and field (up to 140 kOe) dependence of magnetization measurements was determined using the vibrating-sample magnetometer option of a physical property measurement system (PPMS) from Quantum Design. High-temperature heat capacity measurements (2–300K) were also performed using the same PPMS. The low-temperature $C_p(T)$ measurements down to 90 mK were performed using a dilution refrigerator attached to the Dynacool PPMS from Quantum Design. QMC simulations were performed using the worm stochastic series expansion (SSE) algorithm [28,29] as implemented in the ALPS package [30].

III. RESULTS AND ANALYSIS

A. Structural characterization

We characterized our sample using powder XRD. The measured XRD is well matched with the calculated pattern generated from the crystallographic information file [31] and is confirmed to be the single phase of $NaCuIn(PO_4)_2$. The values for refinement are as follows: $\chi^2 \approx 2.87$, $R_p \approx 12.4\%$, $R_{wp} \approx 12.6\%$, $R_{exp} \approx 7.44\%$. The obtained lattice parameters from the refinement at room temperature are $a = 8.256$ Å, $b = 10.139$ Å, $c = 8.806$ Å, and $\beta = 114.4°$, which are in close agreement with a previous report [31].

B. Structural analysis

$NaCuIn(PO_4)_2$ crystallizes in the monoclinic space group $P2_1/n$ [31]. The crystal structure is displayed in Fig. 1(a). The principal building units of this phosphate are PO_4 tetrahedra, a CuO_5 triangular bipyramid, an InO_6 octahedron, and a distorted NaO_4 polyhedron. Two adjacent CuO_5 units meet at their edges to form a spin dimer via the NN coupling [indicated by J_1 in Fig. 1(d)]. The bond angle of Cu-O-Cu for the J_1 path is 97.6°, which is close to 90°. This superexchange interaction favors weak antiferromagnetic coupling as per the Goodenough-Kanamori rules [32]. The second-NN coupling between Cu atoms is through PO_4 units forming the spin chains [indicated by J_2 in Fig. 1(d)]. In this bonding, there is a possibility of the magnetic path Cu-O1-O3-Cu. As this path is involved with a shorter bond length for O1-O3 of about 2.53 Å, the J_2 magnetic coupling is expected to be stronger in this compound.

The combination of intrachain (J_2) and interchain (J_1) connections creates the 2D distorted honeycomb structure [see Fig. 1(c)]. The interlayer separation between two honeycomb layers is about 6.91 Å [see Fig. 1(b)]. In each layer, the first-NN Cu^{2+} atoms are connected to each other with a path length of 3.09 Å, and the Cu^{2+} dimers are coupled to each other with a path length of 5.32 Å [see Fig. 1(d)]. The details of the possible magnetic couplings are summarized in Table I. When the third-NN coupling J_3 is considered, we can view

TABLE I. The details of the bond path, bond length, and bond angle of the magnetic couplings for $NaCuIn(PO_4)_2$.

Coupling	Bond path	Bond length (Å)	Bond angle (deg)
J_1	Cu-O8-Cu	3.09	Cu-O8-Cu = 97.6
J_2	Cu-O1-O3-Cu	5.32	Cu-O1-O3 = 153.6, O1-O3-Cu= 104.9
J_3	Cu-O2-In-O3-Cu	6.09	Cu-O2-In = 121.2, In-O3-Cu = 129.1

it as a 2D distorted Shastry-Sutherland lattice. However, the J_3 coupling seems to be weak because it has a longer bond distance compared to J_1 and J_2 and because of the heavier element (InO_6 unit) involved. These possible magnetic exchange interactions will be further verified by the analysis of the magnetic susceptibility results.

C. Magnetization measurements

The temperature-dependent magnetic susceptibility $\chi(T)$ of the polycrystalline sample $NaCuIn(PO_4)_2$ is measured as shown in Fig. 2(b). The occurrence of a broad maximum at 13 K in $\chi(T)$ is the characteristic feature of low-dimensional quantum magnetic systems. The $\chi(T)$ data are fitted to the Curie-Weiss law in the temperature range of 20–300 K:

$$\chi = \chi_o + \frac{C}{T - \theta_{CW}}, \tag{1}$$

where C is the Curie constant, χ_o is the temperature-independent susceptibility, and θ_{CW} is the typical Curie-Weiss temperature. The parameters obtained from the fit in Fig. 2(a) for $T \geqslant 20$ K are the temperature-independent magnetic susceptibility $\chi_o \simeq -1.23 \times 10^{-4}\,\mathrm{cm^3/mol}$, which is the sum of the core diamagnetic susceptibility χ_{dia} and Van Vleck susceptibility χ_{VV}; $C \simeq 0.5\,\mathrm{cm^3 K/mol}$; and $\theta_{CW} \approx -16$ K. A negative value of θ_{CW} indicates that the dominant interactions between the Cu^{2+} ions are AFM in nature. Adding the core diamagnetic susceptibilities of the individual ions Na^+, Cu^{2+}, P^{5+}, and O^{2-} [33], we get $\chi_{dia} \simeq -1.33 \times 10^{-4}\,\mathrm{cm^3/mol}$ for the compound $NaCuIn(PO_4)_2$. Deducting χ_{dia} from χ_o gives us the χ_{VV}, which is determined to be $\simeq 0.1 \times 10^{-4}\,\mathrm{cm^3/mol}$, resulting from the second-order contribution to the free energy in the presence of the magnetic field. Assuming the Landé g factor $g = 2$, the spin-only effective moment for an $S = \frac{1}{2}$ system is predicted to be $\mu_{eff} = g\sqrt{S(S+1)}\,\mu_B \approx 1.73\mu_B$, where μ_B is the Bohr magneton. However, the experimental value of the spin-only effective moment was found to be $\mu_{eff} \approx 2.05\mu_B$, which is calculated with the help of the Curie constant value by using the relation $\mu_{eff} = \sqrt{3k_B C/N_A} \approx \sqrt{8C}\mu_B$, where N_A is Avogadro's number and k_B is the Boltzmann constant. This value of μ_{eff} is slightly larger than the value that is expected for free $S = \frac{1}{2}$ due to the unquenched

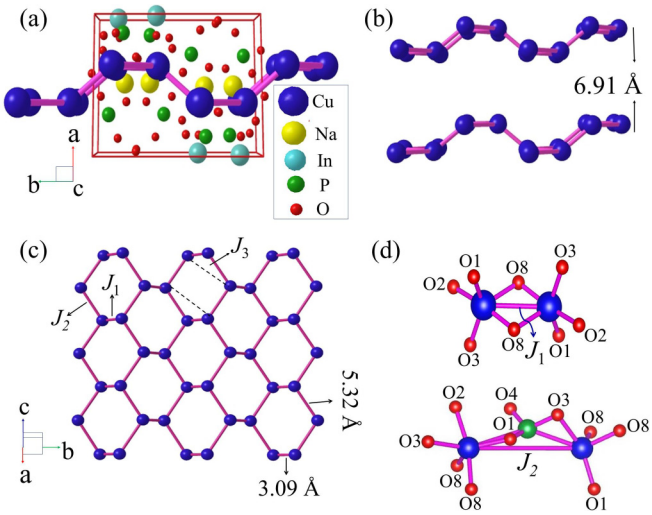

FIG. 1. (a) The crystal structure of $NaCuIn(PO_4)_2$. (b) The interlayer separation between two honeycomb layers is about 6.91 Å. (c) The spin network shows the distorted honeycomb lattice with J_1, J_2, and J_3 couplings. (d) The intrachain interaction paths for first-NN (J_1) and second-NN (J_2) couplings.

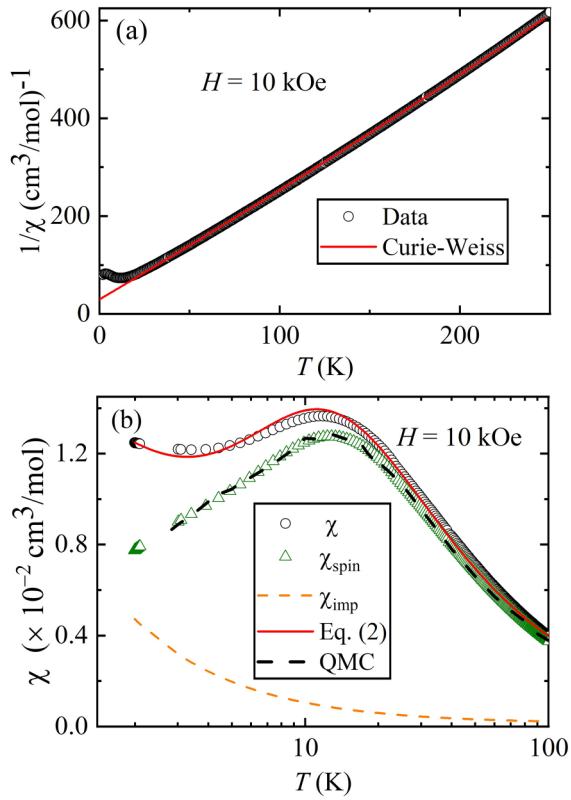

FIG. 2. (a) The inverse magnetic susceptibility $1/\chi$ vs temperature T. The solid red line indicates the fit to the Curie-Weiss law. (b) The measured magnetic susceptibility χ data are shown by black open circles as a function of T in an applied field of 10 kOe. The red solid line is the best fit using Eq. (2). The yellow dashed line represents the impurity contribution $\chi_{imp}(T)$. The spin susceptibility $\chi_{spin}(T)$ is obtained by subtracting $\chi_{imp}(T)$ from the measured $\chi(T)$. The black dashed line illustrates the rescaled magnetic susceptibility as simulated by QMC.

spin-orbit coupling and has been noticed in several Cu^{2+}-based compounds [34]. Furthermore, we typically divide $\chi(T)$ into three components,

$$\chi(T) = \chi_o + \frac{C_{\rm imp}}{T + \theta_{\rm imp}} + \chi_{\rm spin}(T). \quad (2)$$

Here, the second term indicates the concentrations of paramagnetic impurities, where the interaction strength between the impurity spins is given by $\theta_{\rm imp}$.

$\chi_{\rm spin}(T)$ denotes the intrinsic spin susceptibility of the spin network [see Eq. (3)]. The fitting expression used for $\chi(J_2, T)$ is explained in the Appendix. From the structural point of view, we noted that the title compound might have a combination of J_1 and J_2 couplings. Since the experimental magnetic susceptibility does not fall exponentially to zero, there is less possibility of having dominant J_1 coupling. We then considered J_2 to be the dominant coupling based on the structural predictions. In order to understand the exchange coupling strengths in the compound, we naively assumed and fitted the magnetic susceptibility data with the $S = \frac{1}{2}$ coupled uniform chain model using the mean-field approach [Eq. (2)] down to 2 K:

$$\chi_{\rm spin}(T) = \frac{\chi(\mathrm{J}_2, T)}{1 + \frac{zJ'}{Ng^2\mu_B^2}\chi(\mathrm{J}_2, T)}. \quad (3)$$

The best fit yields values of $C_{\rm imp} \approx 0.0091\ \mathrm{cm^3\,K/mol}$ and $\theta_{\rm imp} \approx 0.65\ \mathrm{K}$. The value of $C_{\rm imp}$ corresponds to an impurity concentration of nearly 2.5% of $S = \frac{1}{2}$ impurity spins. One of the sources for the impurity could be due to the presence of orphan spins. The values of uniform intrachain coupling J_2 and the total strength of interchain coupling zJ' are found to be 18 ± 0.3 and $7.5 \pm 0.2\ \mathrm{K}$, respectively [35]. Here, z represents the number of nearest-neighbor spin chains. In general, the z value is 2 for a square-type lattice and 1 for a honeycomb-type lattice. In the view of the $NaCuIn(PO_4)_2$ structure, the interchain coupling strength is $zJ' = z_1J_1 + z_3J_3$, where the coupling strength J_3 is quite weak and is considered to be zero. From the above analysis, J_1 is extracted as $7.5 \pm 0.2\ \mathrm{K}$, which confirms that the interchain interactions in the structure are significant. The intrinsic $\chi_{\rm spin}(T)$ of $NaCuIn(PO_4)_2$ is obtained after subtracting the temperature-independent and paramagnetic impurity contributions from the measured $\chi(T)$, as also shown in Fig. 2(b). The magnetic susceptibility $\chi(T)$ was calculated using QMC simulations on an $S = \frac{1}{2}$ distorted honeycomb spin lattice model taking into account the exchange couplings J_1 and J_2 as indicated in Fig. 1(c). The calculations using a four-Cu-spin unit cell were run on $L \times L$ lattices of $L = 20$, i.e., containing 1600 spins. As depicted in Fig. 2(b), the simulated data quite nicely reproduce $\chi_{\rm spin}(T)$ in the temperature range of $T = 2$–$100\ \mathrm{K}$ with values of $J_1 \approx 7.6\ \mathrm{K}$ and $J_2 \approx 20\ \mathrm{K}$.

The ratio of the exchange couplings obtained with the QMC simulations ($\frac{J_2}{J_1} \approx 2.63$) is nearly consistent with the experimental analysis. Our result indicates that the chains are coupled within the 2D plane, forming the 2D distorted J_1-J_2 honeycomb lattice. The linear behavior of $M(H)$ at 2 K, as presented in Fig. 3, indicates the absence of ferromagnetic impurities in the samples. $M(H)$ data do not saturate up to an applied magnetic field of 140 kOe. At 140 kOe, the $M/M_{\rm sat}$ value reaches only 0.3, which means that a large magnetic field of about 40 T is required for the full saturation of a magnetic moment of $1\mu_{\rm B}$ for $S = \frac{1}{2}$ and $g = 2$.

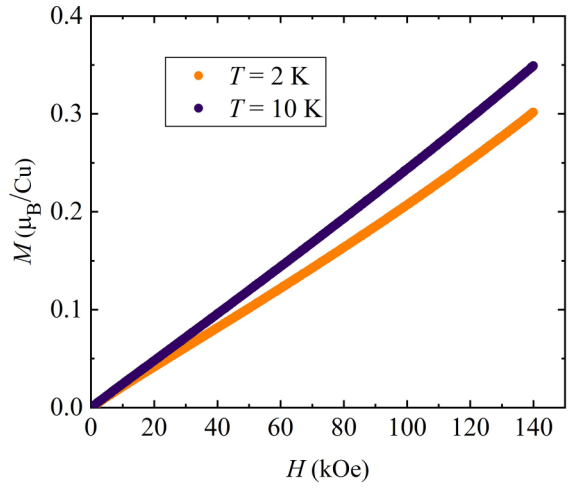

FIG. 3. Magnetic isotherms measured at 2 and 10 K in magnetic fields up to 140 kOe.

D. Heat capacity

The temperature-dependent heat capacity $C_p(T)$ is measured in zero field, as depicted in Fig. 4(a). C_p in magnetic insulators typically has a major contribution from phonon

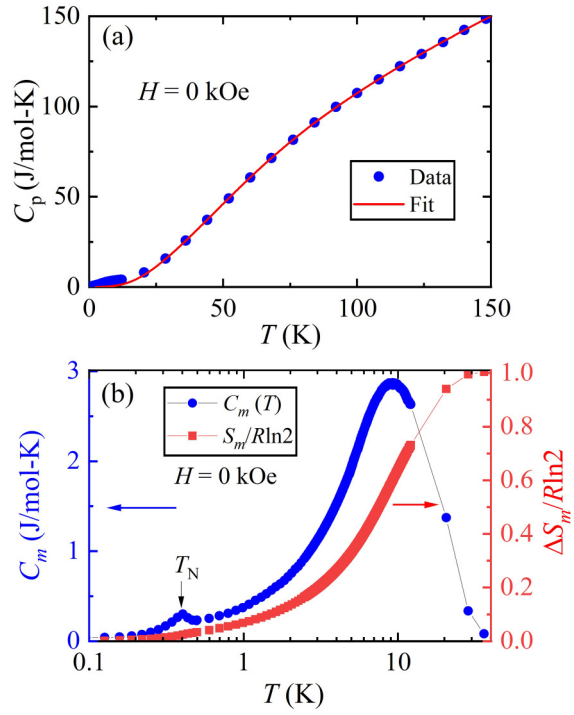

FIG. 4. (a) Variation of heat capacity C_p with respect to the temperature T in zero field. The solid red line reflects the phononic contribution $C_{\rm ph}$. (b) The T variation of magnetic heat capacity C_m and normalized entropy $S_m/R\ln(2)$ on the left and right y axes, respectively.

excitations $C_{\rm ph}$ at higher temperatures. In contrast, the magnetic part of the heat capacity C_m dominates over $C_{\rm ph}$ at low temperatures.

As a result, in magnetic materials with a low-energy scale of exchange coupling, the magnetic part of the heat capacity can be separated from the phononic part by examining C_p in the high-temperature region. To extract C_m from C_p, the phonon contribution was initially estimated by fitting the high-T data with one Debye and two Einstein terms [36]:

$$C_{\rm ph}(T) = f_D C_D(\theta_D, T) + \sum_{i=1}^{2} g_i C_{E_i}(\theta_{E_i}, T). \tag{4}$$

The first term in Eq. (4) represents the Debye model,

$$C_D(\theta_D, T) = 9nR\left(\frac{T}{\theta_D}\right)^3 \int_0^{\frac{\theta_D}{T}} \frac{x^4 e^x}{(e^x - 1)^2}\, dx, \tag{5}$$

where $x = \frac{\hbar\omega}{k_B T}$, ω is the Debye frequency, R is the universal gas constant, and θ_D represents the Debye temperature. The second part in Eq. (4) is known as the Einstein term, which accounts for the flat optical modes of the lattice vibrations:

$$C_E(\theta_E, T) = 3nR\left(\frac{\theta_E}{T}\right)^2 \frac{e^{\frac{\theta_E}{T}}}{\left[e^{\frac{\theta_E}{T}} - 1\right]^2}. \tag{6}$$

The characteristic Einstein temperature is represented by θ_E. The coefficients f_D, g_1, and g_2 are the multiplication factors that take into account the number of atoms per formula unit n. The zero-field $C_p(T)$ data are fitted using Eq. (4) [see the solid red curve in Fig. 4(a)], and the obtained parameters are $f_D \approx 0.22$, $g_1 \approx 0.27$, $g_2 \approx 0.45$, $\theta_D \approx 189$ K, $\theta_{E1} \approx 299$ K, and $\theta_{E2} \approx 758$ K. Finally, $C_m(T)$ was estimated by extrapolating the high-T fit down to 90 mK and subtracting it from the $C_p(T)$ data. In many low-dimensional magnetic materials, it has been noticed that the broad maximum in the heat capacity is often found at lower temperatures than the broad maximum in $\chi(T)$ [37,38]. The presence of a broad maximum in the heat capacity data can be attributed to short-range spin correlations. A small peak is noticed at $T_N = 0.4$ K, indicating the presence of magnetic LRO. The large value ($\simeq$40) of the ratio of $|\theta_{\rm CW}|$ and T_N suggests that the system has very weak interlayer coupling. We evaluated the change in magnetic entropy ΔS_m from the integration of $C_{\rm m}/T$ versus T. The obtained value of ΔS_m saturates at 32 K. It approaches a value of 5.68 J/mol K, which agrees well with the theoretically predicted value $\Delta S_m = R\ln(2S+1) = 5.75$ J/mol K for an $S = \frac{1}{2}$ system. It is found that the entropy value at the transition temperature $T_{\rm N}$ is only 1.5% of the $R\ln 2$ value, which suggests that the transition is very weak AFM in nature. Below $T_{\rm N}$, $C_m(T)$ follows a T^3 behavior, suggesting that the ground state is AFM LRO with magnon excitations.

To understand the nature of the excitations in the ground state, the magnetic heat capacity $C_m(T)$ data in zero field are fitted with the power law in the temperature range $0.5 \leqslant T \leqslant 6$ [see Fig. 5(a)]. The data fit well with the power-law behavior, resulting in an exponent of $\sim$1. The linear behavior of $C_m(T)$ suggests that the excitations in the ground state are gapless. The small deviation from the T^3 behavior at very low temperatures appears to be likely due to paramagnetic impurities, which are common in low-dimensional magnetic materials, for instance, due to edge spins of the lattice. The inset of Fig. 5(a) depicts $C_p(T)$ measured in 0 and 10 kOe; it can be seen that the transition at $T_{\rm N} = 0.4$ K gets completely suppressed with an external applied magnetic field of 10 kOe, which also follows a linear behavior similar to that of the 0 kOe data.

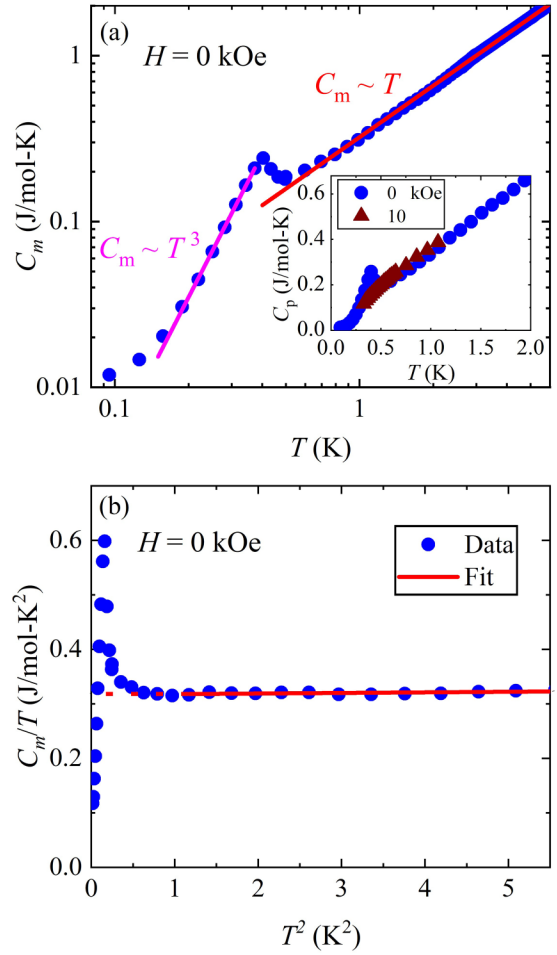

FIG. 5. (a) Magnetic contribution to the heat capacity C_m as a function of temperature T with power-law fits. Inset: The suppression of magnetic LRO in an applied field of 10 kOe. (b) The plot of C_m/T vs T^2 with the $C_m = \gamma T$ fit is shown by the solid red line. The fit is extrapolated by a dashed red line to obtain the γ value.

To understand further, we extracted the linear coefficient γ from the fit to the expression $C_m = \gamma T$, where $\gamma = \frac{2}{3}(\frac{Nk_B^2}{J_{\rm avg}})$ [35]. The experimental γ value is found to be about 0.32 J/mol K^2 [see Fig. 5(b)]. The γ value represents the density of the quasiparticles due to the thermal excitations. The results suggest that the ground state of the $S = \frac{1}{2}$ distorted honeycomb lattice model with $\frac{J_2}{J_1} \approx 2.63$ in the absence of the interlayer interactions might have a quasi-LRO ground state or a disordered ground state in the absence of magnetic frustration. Similar linear behavior and gapless excitations are seen for the $S = \frac{1}{2}$ uniform spin chain model. Interestingly, $J_{\rm avg} \approx 16.5$ K found from $C_m(T)$ is very consistent with the estimated value of $J_{\rm avg} = \frac{(2J_2+J_1)}{3} \approx 15.8$ from the magnetic data analysis. We note that the expression for γ is taken in our

analysis based on the fact that our compound has a coupled uniform chain network forming the 2D distorted honeycomb lattice. However, based on the bulk measurements, we cannot fully explain the physical state of these excitations. Future microscopic experiments such as inelastic neutron scattering, nuclear magnetic resonance, and muon spin rotation could reveal the true nature of the spin excitation spectrum of the title compound.

E. Electronic structure calculations

To account for the electronic structure of $NaCuIn(PO_4)_2$, DFT calculations were performed using the Vienna Ab initio Simulation Package (VASP) [39,40]. Plane-wave calculations were performed within the generalized gradient correction of Perdew, Burke, and Ernzerhof [41] for the exchange-correlation function to figure out the ground state of the title compound. The kinetic energy cutoff was set at 500 eV. The Brillouin zone integration for a $4 \times 3 \times 4$ k mesh was performed using the tetrahedron method of Blöchl [42]. We employed two different methods to calculate the strength of exchange interactions between the neighboring spins. The first method is the total energy calculation method based on calculating the total energy difference between the different configurations where spins are flipped relative to a reference configuration. In our case, the reference configuration is ferromagnetic. The second method is based on hopping parameters, for which we obtain the hopping energies up to third-NN using maximally localized Wannier functions (WFs). These WFs are constructed from the random initial projections for four bands dispersed near the Fermi energy using the WIEN2WANNIER and WANNIER90 codes [43,44] in a nonmagnetic setup. We investigated the relative stability of various magnetic states and discovered that an AFM state with oppositely aligned nearest-neighbor Cu^{2+} spins is the most stable configuration. The generalized gradient approximation (GGA) and the inclusion of Hubbard U within the GGA+U framework were used to obtain the electronic structure of this lowest-energy state and to address the exchange and correlation effects. GGA+U computations were done for three different values of on-site Coulomb interaction of Cu d states, namely, $U = 6$, 8, and 10 eV, in conjunction with the on-site specific exchange parameter. These values of U are within the range suggested in previous studies on Cu-based oxides [45–47]. The computed total and partial densities of states (DOSs) for Cu d and O p states are displayed in Fig. 6.

The total DOS [see Fig. 6(a)] clearly shows that the ground state is insulating with a gap of 2.3 eV; to understand the true nature of the insulating ground state further, we analyze the projected DOS around the Fermi level [see Figs. 6(b) and 6(c)]. Here, we observe that the up channel for Cu d states is completely occupied, while only one down channel is empty, which is observed above the Fermi level. This distribution of Cu d states is already expected because Cu has a 2+ charge state with the nominal $3d^9$ occupation. Hence, according to Hund's rule, the majority d states get completely filled, leaving one minority spin state empty. The gap primarily arises between the majority and minority d states, which are further exchange split due to the formation of local moments on the Cu sites. Thus, the generation of the insulating gap can be

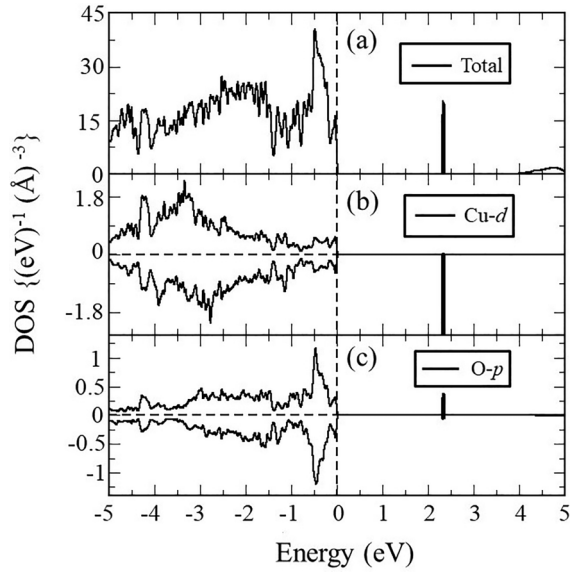

FIG. 6. Density of states (DOS) for the AFM ground state from GGA + U calculations ($U = 6$ eV). (a) Total DOS. (b) Cu d partial DOS. (c) O p partial DOS.

attributed to local magnetic moment formation and the correlation effect of the $3d$ subshell of the Cu ion. The magnetic moment on the Cu^{2+} site is estimated to be $0.72\mu_B$, which is smaller than the moment expected from the nominal $3d^9$ configuration. The quenching of the magnetic moment at the Cu^{2+} site is due to the hybridization with the O p orbitals near the Fermi level. Further, we calculated the magnitudes of exchange couplings between the Cu atoms, J_1, J_2, and J_3, using the total energy method.

The total energies corresponding to various possible magnetic orderings are mapped onto a Heisenberg Hamiltonian [see Eq. (7), where the indices i and j represent the locations of magnetic ions in the unit cell], which gives the relation between various J_{ij} values. Similarly, we consider the total energy for the other configurations and perform our calculation by taking the energy difference with the reference ferromagnetic configuration:

$$H = \sum_{i \neq j} J_{ij} S_i \cdot S_j. \tag{7}$$

The exchange coupling values for different U (on-site interaction) values for Cu d orbitals are shown in Table II, where we give the calculated ratios of various magnetic couplings between Cu atoms for different sets of energies.

TABLE II. The magnetic exchange interactions between the Cu^{2+} ions in $NaCuIn(PO_4)_2$ at different U values extracted from the total energy calculations.

U (eV)	J_1 (meV)	J_2 (meV)	J_3 (meV)	$\frac{J_2}{J_1}$	$\frac{J_3}{J_1}$
6	−1.6	−4.5	−0.2	2.81	0.12
8	−0.9	−2.9	−0.1	3.22	0.11
10	−0.4	−1.8	−0.05	4.50	0.12

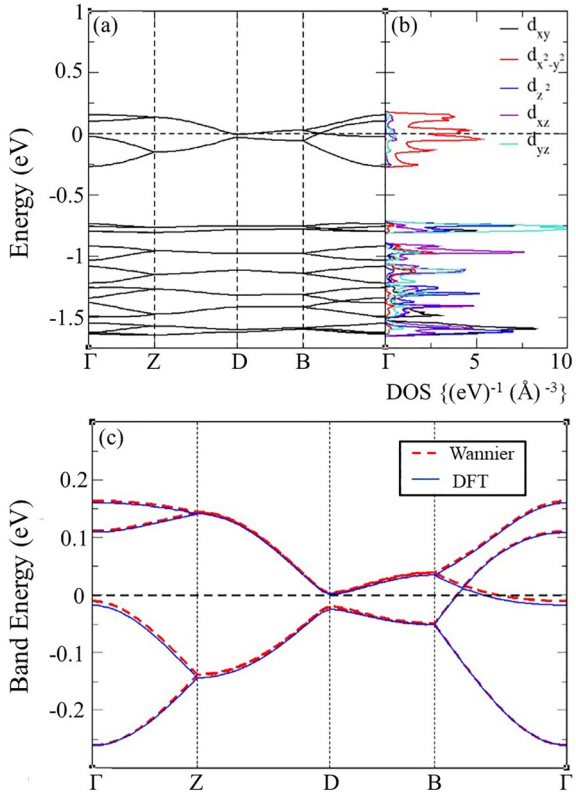

FIG. 7. (a) Non-spin-polarized band dispersion along high-symmetry k points in the first Brillouin zone. (b) The m_l projected partial DOS of the five Cu d orbitals. (c) Wannier-interpolated bands superimposed on the DFT bands.

From the result, it is clear that both NN and second-NN interactions are significant, which essentially forms a distorted honeycomb lattice of $\frac{J_1}{J_2} \approx 0.38$.

Next, we analyze the non-spin-polarized electronic structure to construct a low-energy tight-binding model. Our model is based on maximally localized Wannier functions for the bands around the Fermi level. As we will see below, this procedure helps us to identify the relevant orbitals for magnetic exchange and validates the trend of the interaction strengths, as reported in Table II. Figure 7(a) represents the non-spin-polarized band dispersion along the high-symmetry k path in the first Brillouin zone of the orthorhombic lattice. We can see that four bands are isolated near the Fermi level arising from the four Cu atoms in the unit cell. These four bands have a predominant $d_{x^2-y^2}$ character; see the m_l projected partial density of states in Fig. 7(b). Since Cu is in a nominal d^9 configuration, these isolated bands are half filled and separated from the other Cu d bands. Therefore, by adding a local interaction term U to the Cu $d_{x^2-y^2}$ Wannier functions, one obtains the single-band Hubbard model [48] at half filling, which allows for capturing the insulating ground state of $NaCuIn(PO_4)_2$. Figure 7(c) represents the superposition of interpolated Wannier bands on DFT bands. From this, we obtain hopping interactions t_n, as shown in Table III.

In the strong-coupling limit of the half-filled Hubbard model, the Heisenberg spin exchange is expressed as $J = 4t^2/U$. In Table III, we list the ratio of interatomic magnetic

TABLE III. The magnetic exchange interactions between Cu^{2+} ions extracted from the hopping integrals.

Hopping	Cu-Cu (Å)	Hopping parameters (meV)	$\frac{J_i}{J_1} = (\frac{t_i}{t_1})^2$
t_1	3.09	−43.86	1.00
t_2	5.32	67.22	2.35
t_3	6.09	20.90	0.22

exchange interactions based on the effective hopping strengths t_i. Note that in the past, this method was widely used to estimate interatomic magnetic interaction [37,49–51]. We can see that the exchange coupling values obtained from the total energy method and from the hopping integrals follow the same trend, i.e., J_1 and J_2 are dominant. J_3 is about 3% of J_2 and 15% of J_1. Our calculation suggests that the relative value of J_3 is weak when compared to the relative value of J_2. Hence, the spin network of $NaCuIn(PO_4)_2$ can be considered a distorted honeycomb lattice, agreeing with the crystal structure.

In order to understand the exchange path and reason for the dominant second-NN coupling (J_2 being larger than J_1), we computed the WFs corresponding to the four bands around the Fermi energy, as displayed in Fig. 8(a). The central parts of the WFs are shaped according to $d_{x^2-y^2}$, as expected, and the tails of the Wannier functions sitting at neighboring sites are shaped according to O p_x and p_y symmetry. We did not find any significant weight on the P site. Thus, the tails reflect the fact that the hybridization between the Cu $d_{x^2-y^2}$ and P orbitals is weak. Accordingly, the bonding path between the NN and second-NN Cu ions is schematically explained in Fig. 8(b). The second-NN Cu atom is connected via the Cu-O-O-Cu superexchange path, while the NN is connected by Cu-O-Cu with a bond angle of 97° (close to 90°). Strong hybridization is visible between $d_{x^2-y^2}$, O p_x, and p_y orbitals via sigma

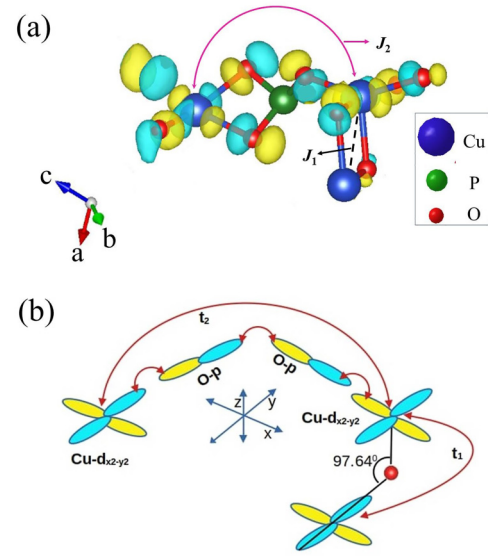

FIG. 8. (a) The Wannier function plot of effective Cu $d_{x^2-y^2}$ orbitals in $NaCuIn(PO_4)_2$. (b) A schematic diagram explaining the superexchange path between the nearest- and next-nearest-neighbor Cu $d_{x^2-y^2}$ orbitals via O p orbitals.

bonding in the same plane. The O-O bonding in the plane mediates the strong second-NN Cu-Cu effective hoppings. Similar O-O bonding plays a key role in another copper oxide material, $SrCuTe_2O_6$, which results in stronger magnetic coupling in the compound [37]. On the other hand, the NN is located in the perpendicular direction, the hybridization strength is much weaker due to π bonding, and hence, the Cu-Cu effective hopping t_1 is also weaker than the second-NN hopping, which is clearly visible from the WF diagram. Thus, the reason for the stronger second-NN magnetic coupling is attributed to the interesting crystal geometry of this system and the symmetry of the orbital ($d_{x^2-y^2}$) responsible for the low-energy physics of this system. Although our Wannierization is based on the effective Cu d WFs and does not include separate WFs for the ligand states such as the O p orbitals, this analysis shows that the spin exchange between the next-NN Cu sites is actually mediated via a superexchange mechanism.

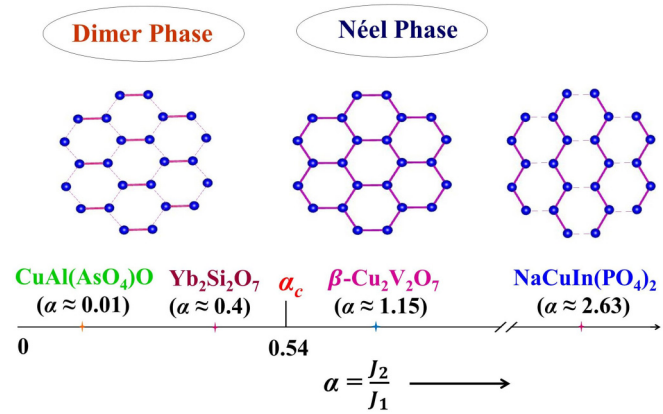

FIG. 9. The quantum phase diagram of the $S = \frac{1}{2}$ HAFM distorted honeycomb lattice separating the spin gap phase and Néel phase as a function of $\alpha = J_2/J_1$.

IV. DISCUSSION

The structure of $NaCuIn(PO_4)_2$ at first glance gives the impression that the NN forms isolated spin dimers, whereas by adding the second-NN and third-NN couplings, the spin network becomes the 2D distorted honeycomb (nonfrustrated) and 2D distorted Shastry-Sutherland (2D frustrated) lattices, respectively. However, through our experimental magnetic data analysis, the possibility of a spin dimer model is ruled out. The failure of the model suggests that J_1 cannot individually describe the spin network of this system completely. So the obvious choice would be the combination of J_1 and J_2, which makes the system a distorted honeycomb lattice. To support this claim, we have analyzed the magnetic susceptibility data with the coupled uniform spin chain model [see Fig. 2(b)]. From the fitting, we obtained $J_1 \approx 7.5 \pm 0.2$ K and $J_2 \approx 18 \pm 0.3$ K. To verify further, we use a more reliable method such as QMC simulations to model the magnetic susceptibility data with an $S = \frac{1}{2}$ distorted honeycomb spin lattice with $J_1 \approx 7.6$ K and $J_2 \approx 20$ K. As depicted in Fig. 2(b), the simulated data quite nicely reproduce $\chi_{\text{spin}}(T)$. The ratio of the exchange couplings obtained through the QMC simulations ($\frac{J_2}{J_1} \approx 2.63$) nearly matches the results of DFT electronic structure calculations. The obtained values of exchange interactions validate the $S = \frac{1}{2}$ distorted honeycomb spin lattice. The theoretical studies suggest a QPD for a 2D distorted honeycomb lattice as a function of the magnetic coupling ratio $\frac{J_2}{J_1}$ (see Fig. 9). This QPD depicts how the distortions in the 2D honeycomb lattice model influence the magnetic behavior, which leads to a quantum phase transition (QPT) from a disordered dimer phase to an AFM ordered Néel phase. QPT from the spin dimer phase to the Néel phase takes place in the proximity of a QCP with $\alpha_c = 0.54$ [10,26].

The position of $NaCuIn(PO_4)_2$ in the QPD along with other compounds is presented in Fig. 9. The compounds $Yb_2Si_2O_7$ ($\alpha \approx 0.4$) [19,20] and $CuAl(AsO_4)O$ ($\alpha \approx 0.01$) [21] are placed in the spin-gapped region. In contrast, the compound β-$Cu_2V_2O_7$ ($\alpha \approx 1.15$) [52] shows the AFM ordering at $T_N = 26$ K and lies on the Néel side of the QPD, as predicted by the 2D HAFM distorted honeycomb lattice model. The value of α for $NaCuIn(PO_4)_2$ is $\approx$2.63, indicating that this material lies on the Néel side of the QPD but in a fairly distant region from the QCP. The material undergoes a magnetic LRO at 0.4 K. The LRO is suppressed by a weak magnetic field of 10 kOe. Above T_N, the magnetic heat capacity follows a linear behavior over a large temperature region, indicating the presence of gapless excitations in the spin excitation spectra. This may be ascribed to the following scenarios: (i) The frustrated magnetic coupling through J_3 ($\frac{J_3}{J_2} \approx 0.03$) could push the LRO to lower temperatures. (ii) The compound has a slightly lower connectivity ($z \approx 2.3$) compared to that of the 2D isotropic honeycomb lattice ($z = 3$), which might induce short-range correlations in the ground state. These factors could contribute to the system being in a ground state with gapless excitations, as evidenced by our results for the $S = \frac{1}{2}$ distorted J_1-J_2 honeycomb lattice $NaCuIn(PO_4)_2$.

V. CONCLUSION

In this work, we have investigated the thermodynamic and magnetic properties of the $S = \frac{1}{2}$ material $NaCuIn(PO_4)_2$. The compound is realized as an $S = \frac{1}{2}$ HAFM 2D distorted honeycomb lattice, which was validated by the results of QMC simulations and the DFT electronic structure calculations. Magnetization and heat capacity studies revealed the presence of short-range correlations typical of low-dimensional spin systems. A weak AFM LRO was noticed at 0.4 K. The magnetic transition was killed by applying a magnetic field of 10 kOe. In addition, $C_m(T)$ follows linear behavior above T_N, indicating that the spin excitations are gapless. These unusual excitations are probably due to the low-connectivity nature and weak magnetic frustration of the distorted honeycomb layers. Overall, the system $NaCuIn(PO_4)_2$ resides on the right side of the QPD, in a far region of the Néel phase, and shows unusual low-energy excitations. Local probe experiments like nuclear magnetic resonance and inelastic neutron scattering at subkelvin temperatures on the single-crystalline form of the material might shed detailed microscopic insights concerning the ground state and spin dynamics.

TABLE IV. The fitting parameters used in the expression of the $S = \frac{1}{2}$ antiferromagnetic uniform chain model [35].

Parameter	$\chi^*(\alpha = 1)$
N_1	−0.24026
N_2	0.45118
N_3	0.01258
N_4	0.03579
N_5	0.00801
N_6	0.00182
N_7	0.00005
N_8	0.00018
N_{81}	1.42347
N_{82}	0.34160
t_1	5.69602
D_1	0.25973
D_2	0.58105
D_3	0.26145
D_4	0.14268
D_5	0.05722
D_6	0.01764
D_7	0.00390
D_8	0.00011

ACKNOWLEDGMENTS

B.K. acknowledges support from DST. T.C. thanks the KREA Faculty Research Fellowships (2022–2023) for providing research grants. Work to carry out experiments in Tallinn was supported by the European Regional Development Fund (Awards No. TK133 and No. TK134) and the Estonian Research Council (Projects No. PRG4 and No. PRG1702). P.K. acknowledges the funding from the Science and Engineering Research Board and the Department of Science and Technology, India, through research grants. B.L. acknowledges the allocation of computer resources by the French Grand Équipement National de Calcul Intensif (GENCI) under Project No. A0110912043.

APPENDIX

The equations used for the $S = \frac{1}{2}$ antiferromagnetic Heisenberg uniform chain model $\chi(J_2, T)$ [35] in the coupled spin chain expression [Eq. (3)] are as follows:

$$\chi(J_2, T) = \frac{Ng^2\mu_B^2}{J_2}\chi^*(t), \tag{A1}$$

$$t = \frac{k_B T}{J_2}, \tag{A2}$$

where $\chi^*(t)$ is the reduced spin susceptibility, t is the reduced temperature, and J_2 is the exchange interaction.

$$\chi^*(t) = \left(\frac{1}{4t}\right)\frac{1 + \left[\sum_{n=1}^{7}\frac{N_n}{t^n}\right] + \frac{4N_8\chi^*_{\log}(t)}{t^8}}{1 + \left[\sum_{n=1}^{8}\frac{D_n}{t^n}\right] + \frac{N_8}{t^9}}. \tag{A3}$$

In the above equation $\chi^*_{\log}(t)$ signifies the logarithmic corrections to the reduced magnetic susceptibility, which are given as follows:

$$\frac{1}{\pi^2}\left[1 + \frac{1}{2\mathcal{L}} - \frac{\ln\left(\mathcal{L} + \frac{1}{2}\right) - N_{81}}{(2\mathcal{L})^2} + \frac{N_{82}}{(2\mathcal{L})^3}\right], \tag{A4}$$

$$\mathcal{L} \equiv \ln\left(\frac{t_1}{t}\right). \tag{A5}$$

The above equations include all the parameters which are given in Table IV.

[1] J. G. Bednorz and K. A. Müller, Possible high T_C superconductivity in the Ba-La-Cu-O system, Z. Phys. B **64**, 189 (1986).

[2] A. N. Vasiliev, O. S. Volkova, E. A. Zvereva, and M. Markina, Milestones of low-D quantum magnetism, npj Quantum Mater. **3**, 18 (2018).

[3] L. Balents, Spin liquids in frustrated magnets, Nature (London) **464**, 199 (2010).

[4] B. Dalla Piazza, M. Mourigal, N. B. Christensen, G. Nilsen, P. Tregenna-Piggott, T. Perring, M. Enderle, D. F. McMorrow, D. Ivanov, and H. M. Rønnow, Fractional excitations in the square-lattice quantum antiferromagnet, Nat. Phys. **11**, 62 (2015).

[5] E. Manousakis, The spin-1/2 Heisenberg antiferromagnet on a square lattice and its application to the cuprous oxides, Rev. Mod. Phys. **63**, 1 (1991).

[6] J. D. Reger and A. P. Young, Monte Carlo simulations of the spin-1/2 Heisenberg antiferromagnet on a square lattice, Phys. Rev. B **37**, 5978 (1988).

[7] J. Richter, J. Schulenburg, and A. Honecker, Quantum magnetism in two dimensions: From semi-classical Néel order to magnetic disorder, Quantum Magn. **645**, 85 (2004).

[8] K. Takano, Spin-gap phase of a quantum spin system on a honeycomb lattice, Phys. Rev. B **74**, 140402(R) (2006).

[9] H. C. Jiang, Z. Y. Weng, and T. Xiang, Accurate Determination of Tensor Network State of Quantum Lattice Models in Two Dimensions, Phys. Rev. Lett. **101**, 090603 (2008).

[10] W. Li, S.-S. Gong, Y. Zhao, and G. Su, Quantum phase transition, $O(3)$ universality class, and phase diagram of the spin-$\frac{1}{2}$ Heisenberg antiferromagnet on a distorted honeycomb lattice: A tensor renormalization-group study, Phys. Rev. B **81**, 184427 (2010).

[11] E. Ghorbani, F. Shahbazi, and H. Mosadeq, Quantum phase diagram of distorted $J_1 - J_2$ Heisenberg S=1/2 antiferromagnet in honeycomb lattice: A modified spin wave study, J. Phys.: Condens. Matter **28**, 406001 (2016).

[12] U. Löw, Properties of the two-dimensional spin-1/2 Heisenberg model on a Honeycomb lattice with interlayer coupling, Condens. Matter Phys. **12**, 497 (2009).

[13] H. Takagi, T. Takayama, G. Jackeli, G. Khaliullin, and S. E. Nagler, Concept and realization of Kitaev quantum spin liquids, Nat. Rev. Phys. **1**, 264 (2019).

[14] S.-H. Baek, S.-H. Do, K.-Y. Choi, Y. S. Kwon, A. U. B. Wolter, S. Nishimoto, J. van den Brink, and B. Büchner, Evidence for a Field-Induced Quantum Spin Liquid in α-$RuCl_3$, Phys. Rev. Lett. **119**, 037201 (2017).

[15] A. Kitaev, Anyons in an exactly solved model and beyond, Ann. Phys. (NY) **321**, 2 (2006).

[16] H. Liu, J. Chaloupka, and G. Khaliullin, Kitaev Spin Liquid in 3*d* Transition Metal Compounds, Phys. Rev. Lett. **125**, 047201 (2020).

[17] G. Jackeli and G. Khaliullin, Mott Insulators in the Strong Spin-Orbit Coupling Limit: From Heisenberg to a Quantum Compass and Kitaev Models, Phys. Rev. Lett. **102**, 017205 (2009).

[18] K. Uematsu and H. Kawamura, Randomness-induced quantum spin liquid behavior in the $S = \frac{1}{2}$ random $J_1 - J_2$ Heisenberg antiferromagnet on the square lattice, Phys. Rev. B **98**, 134427 (2018).

[19] G. Hester, H. S. Nair, T. Reeder, D. R. Yahne, T. N. DeLazzer, L. Berges, D. Ziat, J. R. Neilson, A. A. Aczel, G. Sala, J. A. Quilliam, and K. A. Ross, Novel Strongly Spin-Orbit Coupled Quantum Dimer Magnet: $Yb_2Si_2O_7$, Phys. Rev. Lett. **123**, 027201 (2019).

[20] M. O. Flynn, T. E. Baker, S. Jindal, and R. R. P. Singh, Two Phases Inside the Bose Condensation Dome of $Yb_2Si_2O_7$, Phys. Rev. Lett. **126**, 067201 (2021).

[21] A. N. Vasiliev, O. S. Volkova, E. A. Zvereva, A. V. Koshelev, V. S. Urusov, D. A. Chareev, V. I. Petkov, M. V. Sukhanov, B. Rahaman, and T. Saha-Dasgupta, Valence-bond solid as the quantum ground state in honeycomb layered urusovite CuAl(Aso$_4$)O, Phys. Rev. B **91**, 144406 (2015).

[22] H. Yamaguchi, M. Okada, Y. Kono, S. Kittaka, T. Sakakibara, T. Okabe, Y. Iwasaki, and Y. Hosokoshi, Randomness-induced quantum spin liquid on honeycomb lattice, Sci. Rep. **7**, 1 (2017).

[23] Z. Honda, T. Kodama, R. Kikukawa, M. Hagiwara, T. Kida, M. Sakai, T. Fukuda, T. Fujihara, and N. Kamata, Crystal structure of the spin-1/2 honeycomb-lattice antiferromagnet $Cu_2(pymca)_3(ClO_4)$, J. Phys. Soc. Jpn. **84**, 034601 (2015).

[24] A. Okutani, T. Kida, Y. Narumi, T. Shimokawa, Z. Honda, K. Kindo, T. Nakano, Y. Nozue, and M. Hagiwara, High-field magnetism of the honeycomb-lattice antiferromagnet $Cu_2(pymca)_3(ClO_4)$, J. Phys. Soc. Jpn. **88**, 013703 (2019).

[25] T. Shimokawa, K. Takano, Z. Honda, A. Okutani, and M. Hagiwara, Quantum paramagnetic states in the spin-1/2 distorted honeycomb-lattice Heisenberg antiferromagnet: Application to $Cu_2(pymca)_3(ClO_4)$, Phys. Rev. B **106**, 134410 (2022).

[26] Y. Kono, T. Okabe, N. Uemoto, Y. Iwasaki, Y. Hosokoshi, S. Kittaka, T. Sakakibara, and H. Yamaguchi, Magnetic properties of a spin-1/2 honeycomb lattice antiferromagnet, Phys. Rev. B **101**, 014437 (2020).

[27] J. Rodríguez-Carvajal, Recent advances in magnetic structure determination by neutron powder diffraction, Phys. B (Amsterdam, Neth.) **192**, 55 (1993).

[28] M. Troyer, F. Alet, S. Trebst, and S. Wessel, Non-local updates for quantum Monte Carlo simulations, in *The Monte Carlo Method in the Physical Sciences: Celebrating the 50th Anniversary of the Metropolis Algorithm*, AIP Conf. Proc. No. 690 (American Institute of Physics, Melville, NY, 2003), pp. 156–169.

[29] N. V. Prokof'ev, B. V. Svistunov, and I. S. Tupitsyn, Exact, complete, and universal continuous-time worldline Monte Carlo approach to the statistics of discrete quantum systems, J. Exp. Theor. Phys. **87**, 310 (1998).

[30] A. Albuquerque *et al.*, The alps project release 1.3: Open-source software for strongly correlated systems, J. Magn. Magn. Mater. **310**, 1187 (2007).

[31] E. Benhsina, J. Khmiyas, S. Ouaatta, A. Assani, M. Saadi, and L. E. Ammari, Synthesis and crystal structure of $NaCuIn(PO_4)_2$, Acta Crystallogr.. Sect. E **76**, 366 (2020).

[32] J. B. Goodenough, in *Magnetism and the Chemical Bond* (Wiley-Interscience, New York, 1963).

[33] P. W. Selwood, *Magnetochemistry* (Interscience, New York, 1956).

[34] R. Nath, K. M. Ranjith, J. Sichelschmidt, M. Baenitz, Y. Skourski, F. Alet, I. Rousochatzakis, and A. A. Tsirlin, Hindered magnetic order from mixed dimensionalities in CuP_2O_6, Phys. Rev. B **89**, 014407 (2014).

[35] D. C. Johnston, R. K. Kremer, M. Troyer, X. Wang, A. Klümper, S. L. Bud'ko, A. F. Panchula, and P. C. Canfield, Thermodynamics of spin $S = 1/2$ antiferromagnetic uniform and alternating-exchange Heisenberg chains, Phys. Rev. B **61**, 9558 (2000).

[36] C. Kittel and P. McEuen, *Introduction to Solid State Physics* (Wiley, Hoboken, NJ, 2018).

[37] B. Koteswararao, S. Panda, R. Kumar, K. Yoo, A. Mahajan, I. Dasgupta, B. Chen, K. H. Kim, and F. Chou, Observation of $S = 1/2$ quasi-1D magnetic and magneto-dielectric behavior in a cubic $SrCuTe_2O_6$, J. Phys.: Condens. Matter **27**, 426001 (2015).

[38] S. Guchhait, D. V. Ambika, Q. P. Ding, M. Uhlarz, Y. Furukawa, A. A. Tsirlin, and R. Nath, Deformed spin-1/2 square lattice in antiferromagnetic $NaZnVOPO_4(HPO_4)$, Phys. Rev. B **106**, 024426 (2022).

[39] G. Kresse and J. Hafner, *Ab initio* molecular dynamics for liquid metals, Phys. Rev. B **47**, 558 (1993).

[40] G. Kresse and J. Furthmüller, Efficient iterative schemes for *ab initio* total-energy calculations using a plane-wave basis set, Phys. Rev. B **54**, 11169 (1996).

[41] J. P. Perdew, K. Burke, and M. Ernzerhof, Generalized Gradient Approximation Made Simple, Phys. Rev. Lett. **77**, 3865 (1996).

[42] P. E. Blöchl, O. Jepsen, and O. K. Andersen, Improved tetrahedron method for Brillouin-zone integrations, Phys. Rev. B **49**, 16223 (1994).

[43] A. A. Mostofi, J. R. Yates, Y. S. Lee, I. Souza, D. Vanderbilt, and N. Marzari, wannier90: A tool for obtaining maximally-localised Wannier functions, Comput. Phys. Commun. **178**, 685 (2008).

[44] J. Kuneš, R. Arita, P. Wissgott, A. Toschi, H. Ikeda, and K. Held, Wien2wannier: From linearized augmented plane waves to maximally localized Wannier functions, Comput. Phys. Commun. **181**, 1888 (2010).

[45] V. I. Anisimov, J. Zaanen, and O. K. Andersen, Band theory and Mott insulators: Hubbard U instead of stoner I, Phys. Rev. B **44**, 943 (1991).

[46] S. K. Panda, H. Jiang, and S. Biermann, Pressure dependence of dynamically screened Coulomb interactions in NiO: Effective Hubbard, Hund, intershell, and intersite components, Phys. Rev. B **96**, 045137 (2017).

[47] T. C. Sterling and D. Reznik, Effect of the electronic charge gap on LO bond-stretching phonons in undoped La_2CuO_4 calculated using LDA+U, Phys. Rev. B **104**, 134311 (2021).

[48] J. Hubbard, Electron correlations in narrow energy bands, Proc. R. Soc. A **276**, 238 (1963).

[49] H. Das, U. V. Waghmare, T. Saha-Dasgupta, and D. D. Sarma, Electronic Structure, Phonons, and Dielectric Anomaly in Ferromagnetic Insulating Double Perovoskite La_2NiMnO_6, Phys. Rev. Lett. **100**, 186402 (2008).

[50] S. Baidya, P. Sanyal, H. Das, B. Roessli, T. Chatterji, and T. Saha-Dasgupta, Understanding neutron scattering data in YMn_2O_5: An effective spin Hamiltonian, Phys. Rev. B **84**, 054444 (2011).

[51] S. K. Panda, Y. O. Kvashnin, B. Sanyal, I. Dasgupta, and O. Eriksson, Electronic structure and exchange interactions of insulating double perovskite La_2CuRuO_6, Phys. Rev. B **94**, 064427 (2016).

[52] A. A. Tsirlin, O. Janson, and H. Rosner, β-$Cu_2V_2O_7$: A spin-1/2 honeycomb lattice system, Phys. Rev. B **82**, 144416 (2010).